Anti-VEGF treatment reduces blood supply and increases tumor cell invasion in glioblastoma

Olivier Keunen[a,b], Mikael Johansson[a,c], Anaïs Oudin[a], Morgane Sanzey[a], Siti A. Abdul Rahim[a], Fred Fack[a], Frits Thorsen[b], Torfinn Taxt[b,d], Michal Bartos[e], Radovan Jirik[e,f], Hrvoje Miletic[b,g], Jian Wang[b], Daniel Stieber[a], Linda Stuhr[b], Ingrid Moen[b], Cecilie Brekke Rygh[b], Rolf Bjerkvig[a,b,1], and Simone P. Niclou[a,1,2]

[a]NorLux Neuro-Oncology Laboratory, Oncology Department, Centre de Recherche Public de la Santé, 1526 Luxembourg, Luxembourg; [b]Department of Biomedicine, University of Bergen, 5009 Bergen, Norway; [c]Department of Radiation Sciences, Oncology, Umeå University, 90185 Umeå, Sweden; [d]Department of Radiology, Haukeland University Hospital, 5021 Bergen, Norway; [e]Institute of Scientific Instruments, Academy of Sciences of the Czech Republic, 61264 Brno, Czech Republic; [f]Department of Biomedical Engineering, Brno University of Technology, 61200 Brno, Czech Republic; and [g]Department of Pathology, Haukeland University Hospital, Bergen, Norway

Edited* by George Klein, Karolinska Institute, Stockholm, Sweden, and approved January 21, 2011 (received for review October 6, 2010)

Bevacizumab, an antibody against vascular endothelial growth factor (VEGF), is a promising, yet controversial, drug in human glioblastoma treatment (GBM). Its effects on tumor burden, recurrence, and vascular physiology are unclear. We therefore determined the tumor response to bevacizumab at the phenotypic, physiological, and molecular level in a clinically relevant intracranial GBM xenograft model derived from patient tumor spheroids. Using anatomical and physiological magnetic resonance imaging (MRI), we show that bevacizumab causes a strong decrease in contrast enhancement while having only a marginal effect on tumor growth. Interestingly, dynamic contrast-enhanced MRI revealed a significant reduction of the vascular supply, as evidenced by a decrease in intratumoral blood flow and volume and, at the morphological level, by a strong reduction of large- and medium-sized blood vessels. Electron microscopy revealed fewer mitochondria in the treated tumor cells. Importantly, this was accompanied by a 68% increase in infiltrating tumor cells in the brain parenchyma. At the molecular level we observed an increase in lactate and alanine metabolites, together with an induction of hypoxia-inducible factor 1α and an activation of the phosphatidyl-inositol-3-kinase pathway. These data strongly suggest that vascular remodeling induced by anti-VEGF treatment leads to a more hypoxic tumor microenvironment. This favors a metabolic change in the tumor cells toward glycolysis, which leads to enhanced tumor cell invasion into the normal brain. The present work underlines the need to combine anti-angiogenic treatment in GBMs with drugs targeting specific signaling or metabolic pathways linked to the glycolytic phenotype.

angiogenesis | glioma | metabolism | perfusion

Glioblastomas (GBMs) are highly vascularized brain tumors and are therefore attractive targets for anti-angiogenic therapies (1). In particular, vascular endothelial growth factor (VEGF) has been identified as a critical regulator of angiogenesis, and currently a number of clinical trials targeting the VEGF-signaling pathways are under development (2, 3). Bevacizumab (bev), a humanized anti-VEGF antibody, has shown promising results in exploratory phase II trials of recurrent GBM. Alone or in combination with irinotecan, it is well tolerated and shows a high radiological response rate and possibly an increase in median progression-free survival compared with historical controls (4–7), although no impact on overall survival has been reported (8). However, these results are based on small patient cohorts and, because anti-angiogenic agents directly affect vessel permeability, the imaging response assessment based on contrast enhancement (CE) is highly ambiguous (9). Indeed, a direct antitumor effect of bev has remained elusive and the infiltrative part of the tumor may even increase (10, 11). In addition to a lack of robust clinical data, the cellular and molecular consequences of anti-VEGF treatment have not been outlined (12). Detailed information on how bev affects GBM is important not only to understanding the success or failure of such treatment, but also to providing educated advice on how combination therapies should be optimized.

We have developed a clinically highly relevant human GBM model in rats that fully reflects the growth pattern of human tumors in situ, including extensive infiltration into the brain parenchyma (major pattern of invasion along fiber tracts and blood vessels), prominent angiogenesis, and necrosis (13–15). Comparative genomic hybridization studies have confirmed the genetic similarity between xenografted tumors and the corresponding human tumors (Fig. S1). Thus, our model retains the cellular and genetic heterogeneity that characterizes human GBMs. This is of prime importance for experimental studies, because it is well known that xenograft models based on glioma cell lines poorly reflect the clinical situation. Using our patient-based model system, we have assessed the phenotypic, physiological, and molecular effects of bev treatment in GBMs. We show that anti-angiogenic treatment leads to major vessel remodeling, resulting in reduced perfusion and an increase in hypoxia in the tumor microenvironment. This leads to a metabolic shift in the tumors toward glycolysis, reflected by both an increase in lactate production and a stabilization of hypoxia-inducible factor 1α (HIF1α), and is accompanied by a dramatic increase in cell invasion into the normal brain.

Results

Marked Decrease in Contrast Agent Leakage After Bevacizumab Treatment and a Limited Reduction in Tumor Progression. Three weeks after implantation of patient-derived tumor spheroids, animals were randomly divided into control groups and treatment groups. Bevacizumab was administered through weekly i.v. injections over a 3-wk period. Initial tumor size before treatment was 23.1 ± 9.6 mm^3 (values are reported as mean ± SD, unless otherwise specified) as determined from the visible part (tumor core) of T2-weighted MRI images. After 3 wk of treatment, the tumors in the control group had grown to an average size of 322 ± 176 mm^3, whereas the bev-treated tumors had reached an average size of 230 ± 76 mm^3 (see Fig. 1 *A* and *B* for representative T2-weighted images). The tumor doubling time (TDT) (16) of bev-treated tumors increased by about 16% ($P < 0.05$) compared with untreated tumors, indicating a slowdown of tumor progression during treatment (Fig. 1*C*). Comparable results were obtained with immunohistochemical staining for the proliferation

Author contributions: O.K., M.J., R.B., and S.P.N. designed research; O.K., M.J., A.O., M.S., S.A.A.R., F.F., F.T., H.M., J.W., D.S., C.B.R., L.S., I.M., and R.B. performed research; T.T., M.B., and R.J. contributed new reagents/analytic tools; O.K., M.J., A.O., M.S., S.A.A.R., F.F., F.T., T.T., M.B., R.J., H.M., D.S., R.B., and S.P.N. analyzed data; and O.K., R.B., and S.P.N. wrote the paper.

The authors declare no conflict of interest.

*This Direct Submission article had a prearranged editor.

Freely available online through the PNAS open access option.

[1]R.B. and S.P.N. contributed equally to this article.

[2]To whom correspondence should be addressed. E-mail: simone.niclou@crp-sante.lu.

This article contains supporting information online at www.pnas.org/lookup/suppl/doi:10.1073/pnas.1014480108/-/DCSupplemental.

marker Ki67, indicating a small but significant reduction of stained nuclei (11% reduction, $P < 0.05$) in the treated animals (Fig. 1 *D–F*). Average tumor apparent diffusion coefficient (ADC) values in the tumor core were statistically unchanged, suggesting that there was no major effect on the cellularity of the tumor. Tumor volumes assessed from postcontrast T1-weighted sequences provided similar values as those assessed from T2-weighted sequences (Fig. 1 *G–I*), indicating a reliable estimation of tumor volume independent of CE and suggesting a limited amount of edema in our model. As expected, T1-weighted images obtained after injection of contrast agent and quantification of the area under the curve (AUC) from the dynamic T1-weighted images revealed a significant reduction (34%, $P < 0.05$) in CE in the bev-treated group (Fig. 1 *J–L*). This is in full agreement with reported clinical data (4, 17, 18). In summary, these data indicate that, in our xenograft model derived from patient tumor material, bev induces a slight reduction in tumor progression during the treatment period and strongly reduces leakage of contrast agent from the blood vessels.

Bevacizumab Reduces Tumor Blood Flow and Blood Volume and Affects Vessel Permeability Parameters. To address the physiological consequences of bev on the tumor vasculature and gain insight into the CE changes observed, we performed dynamic contrast-enhanced MRI (DCE-MRI). In this technique, the temporal changes in contrast consecutive to the bolus injection of the contrast agent are recorded and fed to a pharmacokinetic multicompartmental model from which perfusion and permeability parameters are estimated. Several existing models differ in the number of available parameters, complexity, and stability. Thus, the Tofts model (19), which is often used in clinical settings, provides access to three independent parameters [blood or plasma volume (v_b), extravascular extracellular space fraction (v_e), and blood-to-tissue transfer constant (K_{trans})]. The tissue homogeneity model (20) used in this study provides the additional parameter of blood flow. Interestingly, we observed in bev-treated animals a 17% reduction in tumor blood flow (F_b, $P < 0.01$) (Fig. 2 *A–C*) and a 46% reduction in blood volume per unit of tissue (v_b, $P < 0.001$) (Fig. 2 *D–F*), suggesting a reduced supply of oxygen and nutrients to the tumor. As expected from the reduced CE seen on radiological images (Fig. 1 *J–L*), several permeability parameters were significantly reduced by the treatment: K_{trans} (33% reduction, $P < 0.001$) (Fig. 2 *G–I*), permeability surface (PS), extraction fraction (E), and the tissue-to-blood backflow constant (k_{ep}). No significant changes were detected in the v_e fraction (Fig. 2 *J–L*).

Using statistical analysis of variance, we determined the origin of the variability of the perfusion parameters: although tumor size and animal weight contributed to the variation, the treatment itself had a distinct statistically significant effect on the reduction of blood flow, blood volume, transit time, permeability surface area, and K_{trans}. Similar trends for v_b, K_{trans}, k_{ep}, and v_e were also observed when the Tofts model was used instead of the tissue homogeneity model, thus establishing that the changes in perfusion parameters resulted from the treatment effect independent of the model used. Taken together, these data dem-

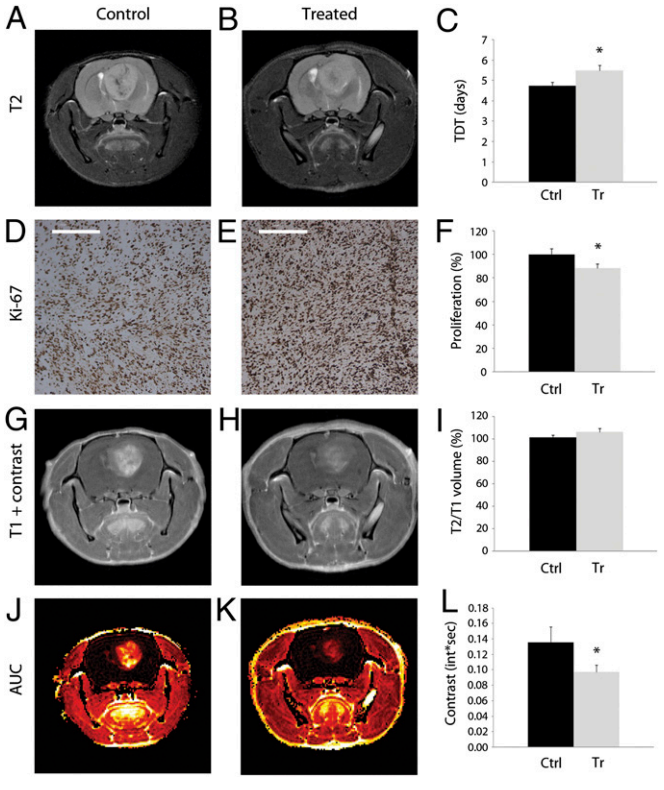

Fig. 1. Quantification of tumor progression and contrast enhancement. Representative images of control (*A*, *D*, *G*, and *J*) and bev-treated animals (*B*, *E*, *H*, and *K*). Tumor volume was assessed from T2-weighted images (*A* and *B*) to determine tumor doubling time (TDT) (*C*), Ki67 immunostaining (*D* and *E*), and quantification thereof (*F*). Control values were set at 100%. (*G* and *H*) Postcontrast T1-weighted images. (*I*) Tumor volumes assessed from postcontrast T1-weighted images were similar to T2-weighted images. (*J–L*) Reduction of contrast agent uptake (CE) in the treated group as evidenced by the mean tumor area under the curve (AUC). Ctrl: controls; Tr: treated. (Scale bars: ±SE.) $*P < 0.05$.

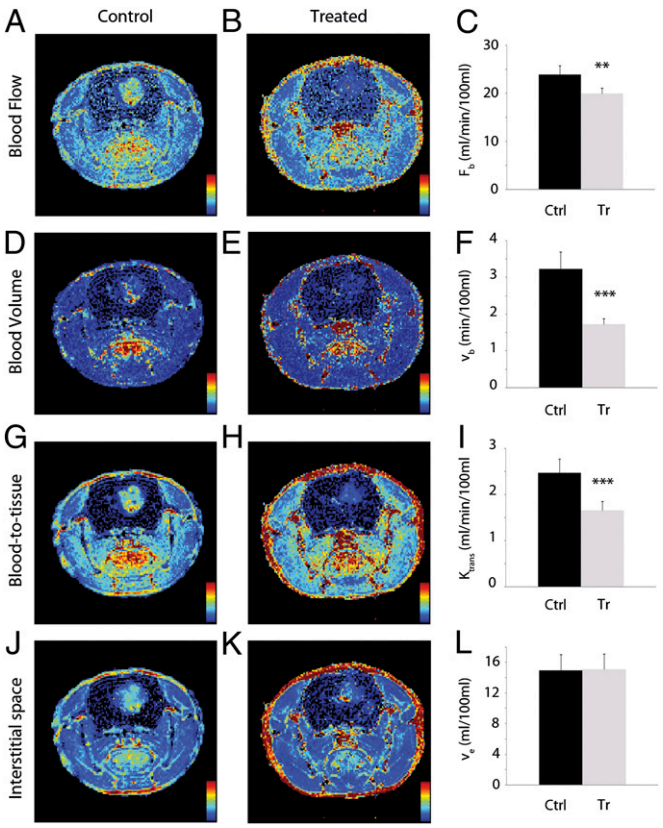

Fig. 2. DCE-MRI analysis of bev-treated glioblastomas. Tumor perfusion maps of representative control (*A*, *D*, *G*, and *J*) and bev-treated animals (*B*, *E*, *H*, *K*). Bevacizumab led to a significant reduction of blood flow, F_b (*A–C*); of blood volume per unit of tissue, v_b (*D–F*); and of the blood-to-tissue extraction constant, K_{trans} (*G–I*). (*J–L*) The extravascular extracellular space (interstitial space volume) per unit of tissue, v_e, was not significantly modified. Ctrl: controls; Tr: treated. (Scale bars: ± SE.) $*P < 0.05$, $**P < 0.01$, $***P < 0.001$. Colors range from blue (low values) to red (high values).

onstrate that the loss of CE observed after anti-VEGF treatment results not only from reduced vessel permeability but also from a reduction of blood flow. This was rather unexpected as it had been proposed that antivascular therapy leads to a "normalization" of the tumor vasculature at the morphological level, which was thought to be accompanied by increased perfusion and improved tumor blood supply (21). Our data show that, at least in GBM, anti-angiogenic treatment leads to reduced blood supply and consequently reduced oxygenation of the tumor bed. It therefore appears that a "morphological" normalization of the vascular bed is not necessarily accompanied by a "functional" normalization of the vascular supply.

Anti-VEGF Treatment Reduces Vessel Density and Strongly Increases Cell Invasion. Quantification of endothelial cell staining revealed a severe reduction in the number of vessels in the bev-treated animals (Fig. 3 *A*–*C*). In particular, large-sized (58%, $P < 0.001$) and medium-sized (17%, $P < 0.001$) blood vessels were strongly reduced, indicating a strong normalizing effect of the treatment. The number of small-sized vessels with a more regular appearance was not affected (Fig. 3*C*).

To visualize human tumor cells in the rat brain and to determine their distribution outside the tumor core, we used a human-specific nestin staining, a protein expressed by the vast majority of GBM cells (15, 22, 23). Interestingly, treated tumors revealed a more homogeneous morphology compared with the controls (Fig. 3 *D*–*F*). For example, control tumors (Fig. 3*D*) showed abundant areas of necrosis and large blood vessels, which were virtually absent in the treated samples (Fig. 3*E*). Increased tumor homogeneity in the treated samples was also confirmed by T2-weighted MRI images (Fig. 3*F*). Importantly, a strong and highly significant increase in the number of tumor cells invading the normal brain (68%, $P < 0.001$) was measured in the bev-treated group (Fig. 3 *G*–*I*). In addition to the number of invading cells, the distance of infiltrating cells from the tumor core was strikingly higher in bev-treated xenografts. The switch to a more invasive phenotype also correlated with a decrease in apparent diffusion coefficient (ADC) in the tumor periphery of the treated animals, although statistical significance was not reached in this parameter. In summary, we show that bev induces a reduction of large- and medium-sized blood vessels, decreases tumor heterogeneity, and results in a dramatic increase in parenchymal tumor cell infiltration.

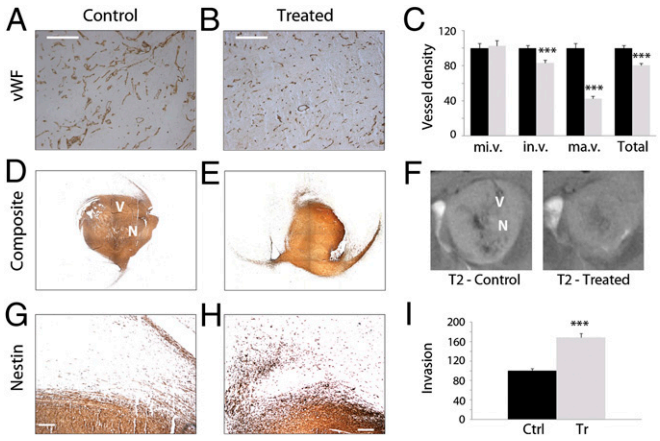

Fig. 3. Changes in blood vessel morphology and tumor cell invasion after bev treatment. Immunostaining for von Willebrand factor (vWF) (*A* and *B*) and quantification thereof (*C*), indicating a significant reduction in the density of medium and large blood vessels and in total vessel number after bev treatment. (Scale bar: 200 μm.) Nestin-stained composite images (*D* and *E*) reveal a more homogeneous appearance of the treated compared with untreated tumors, also reflected in corresponding T2-weighted MRI images (*F*). Large vessels ("V") appear as dark tortuous lines in nestin and T2-weighted images and necrotic areas ("N") as brighter spots. Quantification of the nestin-positive cells outside the tumor core (*G* and *H*) shows a 68% increase in cell invasion after treatment (*I*). mi.v: microvessels; in.v: intermediate-sized vessels; ma.v: macrovessels; Ctrl: controls; Tr: treated. (Scale bars: ± SE.) ***$P < 0.001$.

Histological and Ultrastructural Changes Induced by Bevacizumab Treatment. The untreated xenografts displayed typical hallmarks of GBM, indicated by pseudopalisading necrotic areas and microvascular proliferations in the tumor center and in the periphery (Fig. 4 *A* and *C*). In comparison, treated tumors were mostly devoid of these features, the vessels displayed a nonproliferating endothelium, and the cell density in the tumor periphery seemed reduced (Fig. 4 *B* and *D*). Transmission electron microscopy revealed, in the untreated tumors, a strong activity of the vascular endothelium with sprouting processes (Fig. 4*E*). In comparison, the blood vessels in the treated tumors were more normalized with less visible sprouts (Fig. 4*F*). However, no apparent signs of astrocytic end-feet were seen in these vessels, indicating that the reconstitution of the blood–brain barrier may not be complete. In the tumor core, the treated tumors showed micro-areas of cell lysis indicative of cell death (Fig. 4 *G* and *H*). Quantification of the number of mitochondria revealed a strong reduction of mitochondria in the tumor cells after bev treatment (Fig. 4*I*). Interestingly, ultrastructural analysis of the invasive front, in contrast to the tumor core, showed more homogeneous, rather loosely connected tumor cells (Fig. 4*J*). In summary, we found a loss of endothelial cell proliferation in bev-treated tumors and a reduced number of mitochondria in the tumor cells, which may be a consequence of reduced tumor oxygenation.

Increased Tumor Hypoxia and Activation of the PI3K- and Wnt-Signaling Pathways After Anti-VEGF Treatment. We have previously shown that the infiltrative cells within GBMs show a tendency toward anaerobic glycolysis indicated by increased lactate production (24). In bev-treated tumors, MR spectroscopy showed a tendency toward an accumulation of lactate, alanine, choline, myo-inositol, creatine, taurine, and mobile lipids (Table S1), a combination that has previously been associated with increased hypoxia in human brain tumor spectra (25). Increased lactate levels were also confirmed by proton NMR. Western blot analysis revealed an increase in HIF1α protein in the treatment group compared with the untreated samples (Fig. 5 *A* and *B*), which was also confirmed at the mRNA level (Table S3).

Gene expression analysis of the xenografts further revealed, after treatment, an up-regulation of gene transcripts involved in the phosphoinositol-3-kinase (PI3K)- and Wnt-signaling pathways (Table S2). In fact, from 84 genes related to the PI3K/Akt pathway, 44 were up-regulated more than 1.5-fold after bev treatment, and only one gene was down-regulated in the same order of magnitude. Although not all genes were statistically significant (Table S2) and some negative regulators of the pathway were induced (PTEN, TSC1/2), overall there seems to be a clear trend toward activation of the pathway (Fig. 5*C*). Interestingly, a similar trend was seen for the Wnt pathway, which we have previously found to be induced in the infiltrative compartment of GBMs (13). PCR analysis also indicated that, as a result of bev treatment, the tumor up-regulates several angiogenesis-related transcripts, suggesting an induction of alternative angiogenic pathways (Table S3). These include angiopoietin 2, prostaglandin-endoperoxide synthase 1, urokinase, endothelial tyrosine kinase, and VEGF-A (Table S3). In summary, we show that, in GBM xenografts, bev increases tumor hypoxia and activates alternative angiogenic pathways and molecular functions associated with stem cell biology and the invasive phenotype.

Discussion

Glioblastomas are highly vascularized tumors and therefore represent attractive targets for anti-angiogenic therapies. Despite impressive radiological responses on CE T1-weighted MRI images

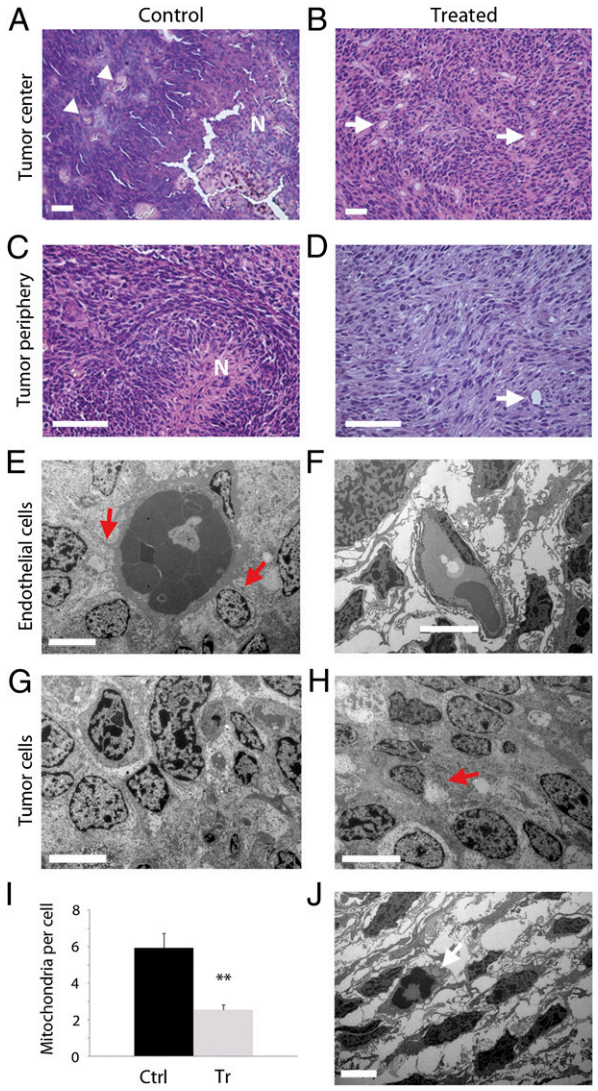

Fig. 4. Histological and ultrastructural changes after bev treatment. Hematoxylin- and eosin-stained sections of GBM xenografts (*A–D*). In control tumors (*A* and *C*), typical hallmarks of GBM growth are visible: necrosis ("N") and microvascular proliferations (arrowheads) in the tumor center (*A*) and periphery (*C*), but not in treated tumors (*B* and *D*). The endothelium appears more normal in treated tumors (arrows). [Scale bar (*A–D*): 50 μm.] (*E–H* and *J*) Transmission electron microscopy (TEM) images of GBM xenografts. Microvascular proliferation and endothelial cell sprouting (red arrows) in control tumors (*E*). Treated tumors show more normalized blood vessels, yet no mature blood–brain barrier (*F*). A denser cellular composition in the tumor core in control tumors (*G*) compared with the treatment group (*H*) where several lytic areas were observed (red arrow). Cells from the invasive front (*J*) had a more elongated morphology, suggesting a subpopulation within the tumor. Dividing cells in the invasive front (white arrow in *J*). [Scale bar (*E–H* and *J*): 5 μm.] Quantification of mitochondria per cell from TEM micrographs (*I*). Ctrl: controls; Tr: treated. (Scale bars: ±SE.) $^{**}P < 0.01$.

in bev-treated patients, tumor cell invasion and recurrence remain major challenges. Thus, there is a strong need to improve treatment strategies for glioblastoma and to better understand the mechanisms of failure for the targeted anti-angiogenic therapies. Here we address these mechanisms by using clinically highly relevant GBM xenografts. Our data show that anti-VEGF treatment induces the loss of large-sized vessels, a dramatic increase in tumor cell invasion, and a significant reduction in tumor blood flow and blood volume. An in-depth quantification of the physiology of the tumor vasculature further revealed a reduction in several permeability parameters, including K_{trans}, k_{ep}, the permeability surface area PS, and the extraction fraction E. Increased tumor hypoxia after anti-VEGF treatment is suggested by induction of HIF1α (both at the gene and the protein level) and an increase in glycolytic metabolites (e.g., lactate). This was accompanied by an up-regulation of the PI3K- and Wnt-signaling pathways. Interestingly, we also detected up-regulation of several angiogenesis-related genes, including VEGF-A. However, the ligand is likely to be efficiently cleared by the excess of drug, and additional compensatory angiogenic factors, although maintaining existing endothelial cells, appear not sufficient to induce neoangiogenesis and to increase blood flow. It should be noted that the xenografts used in the present study carry a typical genetic GBM signature such as amplification of chromosome 7 including EGFR; deletion of CDKN2A/B and loss of one copy of chromosome 9; hemizygous deletion of chromosome 10 including the PTEN gene; and deletion of PI3KR1 (Fig. S1). It is therefore highly unlikely that the observed effects of anti-angiogenic treatment are unique to this particular tumor; however, it cannot be ruled out that certain GBMs respond differently to bev treatment. In view of recent findings indicating that GBMs can contribute to their own vascular supply (26, 27), it will be of interest to determine the VEGF dependency of these tumor-derived endothelial cells and their response to anti-angiogenic treatment.

Bevacizumab is already in clinical use for breast, lung, and colon cancer and appears also promising for the treatment of GBMs. There is, however, a controversy regarding treatment efficacy in terms of patient survival and the validity of radiological response rates as a surrogate endpoint for clinical benefit (9, 27, 28). Furthermore, it is currently not clear whether radiotherapy, which is dependent on the oxygenation level of the tumor, and/or systemic drug delivery, which is influenced by vessel permeability and blood flow, should benefit from anti-angiogenic treatment or not (17). To address these questions, a better understanding of the biological effects of anti-VEGF treatment is mandatory. Detailed analysis of DCE-MRI parameters as performed here was possible due to the use of an advanced pharmacokinetic tissue homogeneity model (20), which, in comparison with the Tofts model traditionally used in the clinical setting (19, 29), provides access to the additional important parameter of blood flow. Because increasing the number of free variables can possibly impact the stability of the model, different measures were taken to optimize the model, among which were the adoption of a good time resolution, the use of local arterial input functions, and a careful monitoring of the model fit (see *SI Materials and Methods* for details). The reduction of CE in T1-weighted images observed after anti-angiogenic treatment can therefore be attributed to a combined effect of a reduction in blood volume, blood flow, and vessel permeability. In agreement with previous reports (30, 31), we propose that static T1-weighted sequences with CE alone are not sufficient to properly assess the efficacy of anti-angiogenic therapies and that perfusion parameters obtained from DCE sequences provide useful additional insight. It should, however, be noted that current models in use have limitations and different applicabilities. Selecting a basic model may provide advantages in terms of simplicity of implementation, but may fail to properly assess the physiological changes induced by the treatment. Diffusion-weighted imaging may have an additional role in assessing changes in cellularity induced by the treatment (32, 33), provided that the causative factors (invasive cells, necrosis, edema) can be distinguished.

Early work from the pioneers of anti-angiogenic treatment suggested that the reduction of newly formed blood vessels starves the tumor from nutrients and oxygen, thereby reducing tumor growth and inducing tumor cell death (starvation hypothesis) (34). It has, however, become clear that the mechanisms of anti-angiogenic therapy are more complex and may also depend on the tumor type (35). For GBMs, at least, induction of tumor cell death has not been demonstrated. More recently, it was proposed that anti-angiogenic treatment leads to blood vessel normalization, thought to be accompanied by increased blood

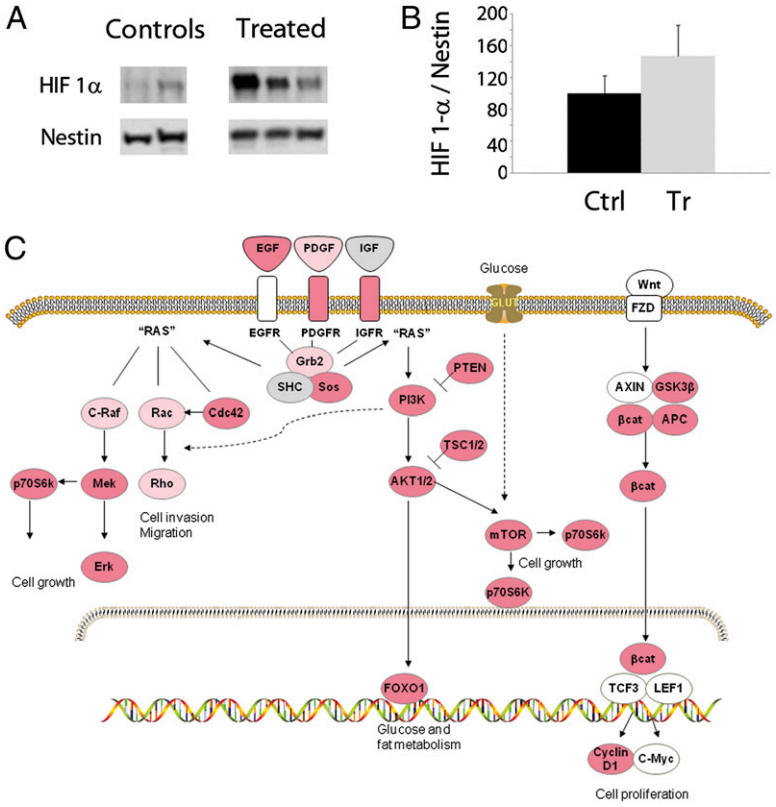

Fig. 5. Molecular changes induced in GBM xenografts after bev treatment. Western blot for HIF1α in control and bev-treated glioblastoma xenografts (*A*) and quantification thereof (*B*). Signal normalization with a human-specific nestin antibody ($n = 7$). (*C*) Schematic of key regulatory molecules associated with receptor tyrosine kinase activation induced after bev treatment (genes marked in dark pink were up-regulated >1.5-fold; genes in light pink were up-regulated >1-fold ; genes in gray were unchanged; and genes in white were not on the array). (Scale bars: ±SE.) $^*P <$ 0.05. (See also Tables S2 and S3.) Ctrl: controls; Tr: treated. AKT1/2: protein kinase B/Bβ; APC: adenomatous polyposis coli; AXIN: axis inhibition protein; βcat: β1 Catenin (CTNNB1); EGFR: epidermal growth factor receptor; Erk: mitogen-activated protein kinase 1 (MAPK1); FOX01: forkhead box O1; FZD: Frizzled homolog; GLUT: glucose transporter; Grb2: growth factor receptor-bound protein 2; GSK3B: glycogen synthase kinase 3 β; IGFR: insuline-like growth factor receptor; LEF1: lymphoid enhancer-binding factor 1; mTOR: FK506 binding protein 12-rapamycin associated protein 1; PDGFR: platelet-derived growth factor receptor; PI3K: phosphoinositide-3-kinase; PTEN: phosphatase and tensin homolog; RAS: RAS protein superfamily; p70s6k: ribosomal protein S6 kinase; SHC: (Src homology 2 domain containing) transforming protein 1; Sos: Son of sevenless; TCF3: transcription factor 3; TSC1/2: tuberous sclerosis 1/2.

flow and oxygenation (normalization hypothesis) (1, 21, 36). In contrast, our data demonstrate a reduction in tumor perfusion and oxygenation in the GBM xenografts. Although increased blood flow might occur during a short normalization window (36), our data suggest that, in GBMs, the long-term effects of anti-VEGF agents are increased hypoxia and increased invasive potential. An anaerobic metabolism is also reflected by an elevation of metabolites associated with glycolysis (Table S1) and the induction of HIF1α protein (Fig. 5). These are phenomena that often correlate with increased invasion and metastasis in solid tumors (37). In this context, it is also interesting to note that we found a significant reduction of mitochondria per cell in bev-treated tumors (Fig. 4*I*).

Enhanced cell infiltration after anti-angiogenic treatment has also been reported in other tumor models (38, 39). Our results further show an up-regulation of the PI3K- and the Wnt-signaling pathways as a result of bev treatment (Fig. 5*C*). These two signaling networks earlier were linked to invasive cells within GBMs (13, 40, 41). Interestingly, the PI3K/Akt pathway is also critically involved in several steps of both anaerobic and aerobic glycolysis regulation, as, for example, in localization of glucose transporters at the cell surface and maintenance of hexokinase function in the absence of extrinsic regulatory factors (40, 42, 43). Thus, activation of Akt as a result of bev-induced hypoxia may increase intracellular glucose and stimulate anaerobic glycolysis and lactate production, thereby promoting invasiveness.

In conclusion, a VEGF blockade causes only a small reduction in tumor burden, but does induce a strong depletion of large- and intermediate-sized blood vessels with a subsequent reduction in vascular leakage and intratumoral blood flow. Anti-VEGF treatment strongly increases tumor cell invasion, which may result from increased hypoxia in the tumor microenvironment. These data are of major clinical importance with regard to combination therapies. For example, our data suggest that radiotherapy, partly dependent on the oxygenation level of the tumor, and systemic drug delivery, influenced by vessel permeability and blood flow, may not profit from coadministered anti-angiogenic treatment in GBM. Bevacizumab is currently approved by the Food and Drug Administration for second-line treatment of GBMs, and new clinical trials aim at assessing its potential in first-line treatment, possibly with additional chemotherapeutic compounds. Our data suggest possible metabolic adaptation mechanisms that might compromise the success of such trials. We propose that anti-angiogenic therapy could benefit from the adjuvent delivery of drugs targeting the HIF1α and PI3K/Akt pathways or by directly interfering with the glycolytic metabolism of tumor cells. Such drugs have recently shown promising results for the treatment of malignant glioma both in experimental models and in patients (44–47).

Materials and Methods

Tumor Material. Patient GBM-derived spheroids (from patient P3) were expanded through serial transplantation in nude rats, thus generating a standardized pool of spheroids (300–400 μm) and giving rise to phenotypically identical (highly invasive and highly angiogenic) GBMs in all xenografts (14). The same genetic aberrations were present in the primary biopsy and in resulting xenografts as determined by array comparative genomic hybridization (Fig. S1). Collection of human biopsy tissue was approved by the regional ethical committee (Haukeland University Hospital, Bergen, Norway).

Intracranial Implantation and Treatment. Ten GBM spheroids were stereotactically implanted into the brain (posterior to the bregma and 3 mm to the right of the midline suture at a depth of 2.5 mm) of 30 athymic nude rats (*rnu–/rnu–*) as described (14). Surgical procedures were in accordance with the Norwegian Animal Act and the local ethical committee. Tumor take was verified by MRI 3 wk post-implantation, and animals were stratified into control ($n = 15$) and treatment groups ($n = 15$). Bevacizumab (10 mg/kg) was given weekly by i.v. injections into the tail vein in accordance with current clinical practice. Control animals were not injected. After 3 wk, rats underwent MRI imaging after which they were killed by perfusion fixation (4% paraformaldehyde/PBS) or by decapitation followed by tumor dissection for RNA isolation, protein extraction, and electron microscopy. No treatment-related adverse effects were observed during the study.

MRI and MRS. MR images were acquired using a 7T Pharmascan small-animal MR scanner (Bruker Biospin) with a linear rat head transmitter/receiver coil. The animals were anesthetized with 1–2% isoflurane mixed with 50% air and 50% O_2 and placed in a prone position in a cradle containing a heating pad at 37 °C. Breathing was monitored throughout. MR sequences used include T2- and T1-weighted images before and after injection of the contrast agent (Gadodiamide, Omniscan; GE Healthcare), diffusion weighted imaging, high-speed DCE-MRI (FLASH sequence with a time resolution of 1.5 s), and ^{1}H MRS. Tumor volumes, TDT, T2/T1 volume ratio (indicative of edema extend), and CE were calculated in nordicICE (NordicNeuroLab) after delineating the tumor on consecutive sections. ADCs were calculated in Paravision 5 (Bruker Biospin). Perfusion and permeability parameters were calculated on the basis of the tissue homogeneity model (20) by using routines custom developed in Matlab (MathWorks). Tumor masks were applied on two consecutive slices of the parameter maps obtained to provide average perfusion parameters. The Tofts model was used for comparison (nordicICE 2.3.4; NordicNeuroLab). Spectra obtained from MRS were processed in LCModel (48) to obtain absolute metabolite concentrations and reported as median values for the treated and control animal groups. For detailed information, see *SI Materials and Methods*.

Immunohistochemistry. Coronal paraffin sections (7–10 μm) were used for histology (hematoxylin/eosin staining) and immunohistochemical analysis: human-specific antibody against nestin (MAB5326; Millipore 1:200), von Willebrand factor (A0082; Dako; 1:200), and Ki67 (M7240; Dako, 1:75). Staining was performed according to the manufacturer's instructions (Envision kit K4011/K4007; Dako). Angiogenesis, invasiveness, and proliferation rate were determined as follows. Stained blood vessels were arbitrarily divided into three classes according to their size. Vessel count indices were computed as a percentage of vessels in treated animals versus controls. Proliferation was assessed by counting KI67-positive cells per section. Invasive potential was assessed by counting nestin-positive invasive cells around the tumor core. For all other experimental procedures, see *SI Materials and Methods*.

ACKNOWLEDGMENTS. We thank A. Muller and P. Nazarov for advice on ingenuity pathway analysis and statistics, respectively, and T. Pavlin and K. Brandt for their assistance in MRI troubleshooting. The project was supported by Centre de Recherche Public de la Santé through a grant from the Ministry of Research and Higher Education in Luxembourg, the Fonds National de la Recherche of Luxembourg; by the Norwegian Cancer Society, the Norwegian Research Council, Innovest AS, Helse Vest, Haukeland University Hospital, and the Bergen Medical Research Fund; and by the Czech Science Foundation (Project Grant GA102/09/1690).

1. Jain RK, et al. (2007) Angiogenesis in brain tumours. *Nat Rev Neurosci* 8:610–622.
2. Reardon DA, Wen PY, Desjardins A, Batchelor TT, Vredenburgh JJ (2008) Glioblastoma multiforme: An emerging paradigm of anti-VEGF therapy. *Expert Opin Biol Ther* 8: 541–553.
3. Miletic H, Niclou SP, Johansson M, Bjerkvig R (2009) Anti-VEGF therapies for malignant glioma: Treatment effects and escape mechanisms. *Expert Opin Ther Targets* 13:455–468.
4. Vredenburgh JJ, et al. (2007) Phase II trial of bevacizumab and irinotecan in recurrent malignant glioma. *Clin Cancer Res* 13:1253–1259.
5. Friedman HS, et al. (2009) Bevacizumab alone and in combination with irinotecan in recurrent glioblastoma. *J Clin Oncol* 27:4733–4740.
6. Vredenburgh JJ, et al. (2007) Bevacizumab plus irinotecan in recurrent glioblastoma multiforme. *J Clin Oncol* 25:4722–4729.
7. Kreisl TN, et al. (2009) Phase II trial of single-agent bevacizumab followed by bevacizumab plus irinotecan at tumor progression in recurrent glioblastoma. *J Clin Oncol* 27:740–745.
8. Norden AD, et al. (2009) An exploratory survival analysis of anti-angiogenic therapy for recurrent malignant glioma. *J Neurooncol* 92:149–155.
9. van den Bent MJ, Vogelbaum MA, Wen PY, Macdonald DR, Chang SM (2009) End point assessment in gliomas: Novel treatments limit usefulness of classical Macdonald's criteria. *J Clin Oncol* 27:2905–2908.
10. Norden AD, et al. (2008) Bevacizumab for recurrent malignant gliomas: Efficacy, toxicity, and patterns of recurrence. *Neurology* 70:779–787.
11. Verhoeff JJ, et al. (2009) Concerns about anti-angiogenic treatment in patients with glioblastoma multiforme. *BMC Cancer* 9:444.
12. Ellis LM, Hicklin DJ (2008) VEGF-targeted therapy: Mechanisms of anti-tumour activity. *Nat Rev Cancer* 8:579–591.
13. Sakariassen PO, et al. (2006) Angiogenesis-independent tumor growth mediated by stem-like cancer cells. *Proc Natl Acad Sci USA* 103:16466–16471.
14. Wang J, et al. (2009) A reproducible brain tumour model established from human glioblastoma biopsies. *BMC Cancer* 9:465.
15. Rajcevic U, et al. (2009) iTRAQ-based proteomics profiling reveals increased metabolic activity and cellular cross-talk in angiogenic compared with invasive glioblastoma phenotype. *Mol Cell Proteomics* 8:2595–2612.
16. Nakajima M, Nakasu S, Morikawa S, Inubushi T (1998) Estimation of volume doubling time and cell loss in an experimental rat glioma model in vivo. *Acta Neurochir (Wien)* 140(6):607–612; discussion 612–603.
17. Norden AD, Drappatz J, Wen PY (2009) Antiangiogenic therapies for high-grade glioma. *Nat Rev Neurol* 5:610–620.
18. Pope WB, Lai A, Nghiemphu P, Mischel P, Cloughesy TF (2006) MRI in patients with high-grade gliomas treated with bevacizumab and chemotherapy. *Neurology* 66: 1258–1260.
19. Tofts PS, et al. (1999) Estimating kinetic parameters from dynamic contrast-enhanced T(1)-weighted MRI of a diffusable tracer: Standardized quantities and symbols. *J Magn Reson Imaging* 10:223–232.
20. Koh TS, et al. (2001) The inclusion of capillary distribution in the adiabatic tissue homogeneity model of blood flow. *Phys Med Biol* 46:1519–1538.
21. Jain RK (2005) Normalization of tumor vasculature: An emerging concept in antiangiogenic therapy. *Science* 307:58–62.
22. Colin C, et al. (2007) Relevance of combinatorial profiles of intermediate filaments and transcription factors for glioma histogenesis. *Neuropathol Appl Neurobiol* 33: 431–439.
23. Kitai R, et al. (2010) Nestin expression in astrocytic tumors delineates tumor infiltration. *Brain Tumor Pathol* 27:17–21.
24. Thorsen F, et al. (2008) Two distinct tumor phenotypes isolated from glioblastomas show different MRS characteristics. *NMR Biomed* 21:830–838.
25. Howe FA, et al. (2003) Metabolic profiles of human brain tumors using quantitative in vivo 1H magnetic resonance spectroscopy. *Magn Reson Med* 49:223–232.
26. Wang R, et al. (2010) Glioblastoma stem-like cells give rise to tumour endothelium. *Nature* 468:829–833.
27. Ricci-Vitiani L, et al. (2010) Tumour vascularization via endothelial differentiation of glioblastoma stem-like cells. *Nature* 468:824–828.
28. Wick W, Weller M, van den Bent M, Stupp R (2010) Bevacizumab and recurrent malignant gliomas: A European perspective. *J Clin Oncol* 28(12):e188–e189; author reply e190–e182.
29. Leach MO, et al.; Pharmacodynamic/Pharmacokinetic Technologies Advisory Committee, Drug Development Office, Cancer Research UK (2005) The assessment of antiangiogenic and antivascular therapies in early-stage clinical trials using magnetic resonance imaging: Issues and recommendations. *Br J Cancer* 92:1599–1610.
30. Hylton N (2006) Dynamic contrast-enhanced magnetic resonance imaging as an imaging biomarker. *J Clin Oncol* 24:3293–3298.
31. Jain RK, et al. (2009) Biomarkers of response and resistance to antiangiogenic therapy. *Nat Rev Clin Oncol* 6:327–338.
32. Chenevert TL, et al. (2000) Diffusion magnetic resonance imaging: An early surrogate marker of therapeutic efficacy in brain tumors. *J Natl Cancer Inst* 92:2029–2036.
33. Gerstner ER, Frosch MP, Batchelor TT (2010) Diffusion magnetic resonance imaging detects pathologically confirmed, nonenhancing tumor progression in a patient with recurrent glioblastoma receiving bevacizumab. *J Clin Oncol* 28:e91–e93.
34. Folkman J (1972) Anti-angiogenesis: New concept for therapy of solid tumors. *Ann Surg* 175:409–416.
35. Ellis LM, Hicklin DJ (2008) Pathways mediating resistance to vascular endothelial growth factor-targeted therapy. *Clin Cancer Res* 14:6371–6375.
36. Batchelor TT, et al. (2007) AZD2171, a pan-VEGF receptor tyrosine kinase inhibitor, normalizes tumor vasculature and alleviates edema in glioblastoma patients. *Cancer Cell* 11:83–95.
37. Gatenby RA, Gillies RJ (2004) Why do cancers have high aerobic glycolysis? *Nat Rev Cancer* 4:891–899.
38. Lucio-Eterovic AK, Piao Y, de Groot JF (2009) Mediators of glioblastoma resistance and invasion during antivascular endothelial growth factor therapy. *Clin Cancer Res* 15:4589–4599.
39. Pàez-Ribes M, et al. (2009) Antiangiogenic therapy elicits malignant progression of tumors to increased local invasion and distant metastasis. *Cancer Cell* 15:220–231.
40. Beckner ME, et al. (2005) Glycolytic glioma cells with active glycogen synthase are sensitive to PTEN and inhibitors of PI3K and gluconeogenesis. *Lab Invest* 85:1457–1470.
41. Ji H, et al. (2009) EGF-induced ERK activation promotes CK2-mediated disassociation of alpha-Catenin from beta-Catenin and transactivation of beta-Catenin. *Mol Cell* 36: 547–559.
42. Bjerkvig R, Johansson M, Miletic H, Niclou SP (2009) Cancer stem cells and angiogenesis. *Semin Cancer Biol* 19:279–284.
43. Robey RB, Hay N (2009) Is Akt the "Warburg kinase"? Akt-energy metabolism interactions and oncogenesis. *Semin Cancer Biol* 19:25–31.
44. Kroemer G, Pouyssegur J (2008) Tumor cell metabolism: Cancer's Achilles' heel. *Cancer Cell* 13:472–482.
45. Pathania D, Millard M, Neamati N (2009) Opportunities in discovery and delivery of anticancer drugs targeting mitochondria and cancer cell metabolism. *Adv Drug Deliv Rev* 61:1250–1275.
46. Michelakis ED, Webster L, Mackey JR (2008) Dichloroacetate (DCA) as a potential metabolic-targeting therapy for cancer. *Br J Cancer* 99:989–994.
47. Michelakis ED (2010) Metabolic modulation of glioblastoma with dichloroacetate. *Sci Transl Med* 2(31):31–34.
48. Provencher SW (2001) Automatic quantitation of localized in vivo 1H spectra with LCModel. *NMR Biomed* 14:260–264.